Research Paper

A Laser-Activated Biocompatible Theranostic Nanoagent for Targeted Multimodal Imaging and Photothermal Therapy

Liming Deng,[1] Xiaojun Cai,[2] Danli Sheng,[1] Yang Yang,[1] Eric M. Strohm,[3] Zhigang Wang,[1] Haitao Ran,[1] Dong Wang,[4] Yuanyi Zheng,[1] Pan Li,[1] Tingting Shang,[1] Yi Ling,[1] Fengjuan Wang,[1] Yang Sun[1],✉

1. Institute of Ultrasound Imaging & Department of Ultrasound, The Second Affiliated Hospital of Chongqing Medical University; Chongqing Key Laboratory of Ultrasound Molecular Imaging, 400010 Chongqing P. R. China;
2. State Key Laboratory of High Performance Ceramics and Superfine Microstructure, Shanghai Institute of Ceramics, Chinese Academy of Sciences 200050, Shanghai, P. R. China;
3. Department of Mechanical and Industrial Engineering, University of Toronto, Toronto M5S 2E8, Canada;
4. Department of Ultrasound, The First Affiliated Hospital of Chongqing Medical University, 400016 Chongqing P. R. China.

✉ Corresponding author: Yang Sun, E-mail: 300006@hospital.cqmu.edu.cn; Tel.:+86-023-63719612.

Abstract

Multifunctional nanoparticles have been reported for cancer detection and treatment currently. However, the accurate diagnosis and efficient treatment for tumors are still not satisfied. Here we report on the development of targeted phase change multimodal polymeric nanoparticles for the imaging and treatment of HER2-positive breast cancer.

Methods: We evaluated the multimodal imaging capabilities of the prepared nanoparticles *in vitro* using agar-based phantoms. The targeting performance and cytotoxicity of the nanoparticles were examined in cell culture using SKBR3 (over-expressing HER2) and MDA-MB-231 (HER2 negative) cells. We then tested the magnetic resonance (MR)/ photoacoustic (PA)/ ultrasound (US)/ near-infrared fluorescence (NIRF) multimodal imaging properties and photothermal effect of the nanoparticles *in vivo* using a SKBR3 breast xenograft model in nude mice. Tissue histopathology and immunofluorescence were also conducted.

Results: Both *in vitro* and *in vivo* systematical studies validated that the hybrid nanoparticles can be used as a superb MR/US/PA/NIRF contrast agent to simultaneously diagnose and guide tumor photothermal therapy (PTT). When irradiated by a near infrared laser, the liquid PFP vaporizes to a gas, rapidly expelling the contents and damaging surrounding tissues. The resulting micro-sized bubbles provide treatment validation through ultrasound imaging. Localization of DIR and SPIO in the tumor region facilitate photothermal therapy for targeted tumor destruction. The mice treated with HER2 targeted nanoparticles had a nearly complete response to treatment, while the controls showed continued tumor growth.

Conclusion: This novel theranostic agent may provide better diagnostic imaging and therapeutic potential than current methods for treating HER2-positive breast cancer.

Key words: multimodality imaging, phase transformation, HER2, theranostic, photothermal therapy

Introduction

Breast carcinoma is the most common cancer threatening women's health and life [1-3]. Common breast cancer screening methods include x-ray mammography, ultrasound (US) and magnetic resonance imaging (MRI) [4]. The effectiveness of cancer screening *via* mammography in reducing the mortality rate from breast cancer has been questionable [5]. US imaging has limited sensitivity in

detection of tumor sizes smaller than 5 mm [6]. MRI exhibits superior sensitivity in small tumor detection, but is not practical for regular screening. Emerging imaging modalities include near infrared fluorescence (NIRF) imaging, which can be used to discriminate diseased tissue from normal tissue, and photoacoustic (PA) imaging, which is an emerging hybrid imaging approach that combines the high contrast and sensitivity of optical imaging with the excellent depth resolution of US imaging [7-9]. These imaging techniques have shown potential in providing valuable morphological and functional information of breast tissues, but haven't demonstrated sufficient specificity and sensitivity for diagnostic screening.

Multimodal imaging, which integrates two or more imaging technologies, can offer more accurate biological details of the tumor. Our group previously synthesized hollow mesoporous prussian blue encapsulated perfluorohexane nanoparticles for US/PA dual-mode imaging, which achieve depth resolution with high optical contrast [10]. Yuanpei Li et al reported porphyrin based nanodots for MR/NIRF imaging for combined functional imaging with tissue structure imaging [11]. Similar contrast agents have been developed for MR/PA imaging, which combines high resolution of MRI and makes up for the limited tissue penetration depth of PA imaging [12]. While these agents have shown promise for diagnostic screening, they have shown limited therapeutic potential.

Recently, photothermal therapy (PTT), which converts light into heat to induce localized tissue damage, has drawn considerable attention in the treatment of cancer [13]. PTT requires external agents to localize the treatment to the tumor tissue, such as gold nanorods [14], graphene [15], and Cu2−xSe nanoparticles [16]. Through irradiation with NIR light, the external agents absorb the energy and increase the temperature within the tissue region. The elevated temperature kills the tumor cells. However, these nanoparticles have low circulation times, are poorly targeted and/or have potential toxic side effects. Therefore, there is an urgent need to develop biocompatible materials to overcome these issues.

Due to their excellent biocompatibility and drug loading capacity, polymer [11, 14, 17], liposome [18] and protein [19-21] materials have been explored as theranostic agents. Through encapsulation with optical absorbers, these biocompatible materials integrate multimodal imaging and PTT technology, simultaneously providing therapeutic function and diagnostic imaging information all in one. Our group previously synthesized perfluorocarbon (PFC) particles for imaging and therapy [22, 23]; through a process called optical droplet vaporization (ODV), the liquid core underwent a phase change to a gas during absorption of light [24, 25]. The resulting bubbles could be used for enhanced ultrasonography, and tumor destruction via vessel occlusion. While promising, their large micron-size and lack of specific targeting were the main barriers hindering their application *in vivo*.

In this study, we have developed theranostic nanoparticles composed of biocompatible materials approved by Food and Drug Administration (FDA) [26-30] for HER2 positive breast cancer diagnosis and therapy. The nanoparticles are 300 nm in diameter, with a poly (lactic-co-glycolic acid) (PLGA) polymer shell encapsulating a perfluoropentane (PFP) liquid core. The liquid PFP core (boiling point 29 °C) exists in a superheated state within the nanoparticle; through ODV, it can be triggered to vaporize to a gas phase through absorption of light [31]. The shell surface was modified with polyethylene glycol (PEG) to prolong blood circulation time and HER2 targeting ligands for targeting HER2 expressing cancer cells. Superparamagnetic iron oxide (SPIO) nanoparticles [32] within the shell enable MR [33-35] and PA [36] imaging. Also contained in the shell is 1,1'-dioctadecyl-3,3,3',3'-tetramethylindotricarbocyanine iodide (DIR), commonly used as a NIRF contrast agent [37]. When irradiated with a near infrared (NIR) laser, the SPIO and DIR in the shell facilitate the ODV process, resulting in a violent expulsion of PFP gas from the particle. The surrounding tissue is damaged, and the resulting microbubbles can be imaged with contrast enhanced ultrasound imaging to verify vaporization occurred [38].

In this study, we demonstrate that the nanoparticles have excellent contrast for identifying HER2-expressing tumors using MRI, PA, and NIRF. The nanoparticles can be activated *via* PTT for precise tumor therapy, and the activation was confirmed through US imaging. This multimodal imaging and therapeutic nanoagent may help with the diagnosis and treatment of HER2 positive breast cancer.

Materials and Methods

Materials

PEGylated Poly (lactic-co-glycolic acid, lactide: glycolide = 50:50, PLGA 20,000 Da MW, PEG 10,000 Da MW) (PLGA-PEG$_{10,000}$) was purchased from the Shan-dong Key Laboratory of Medical Polymer Materials (Shan-dong, China). Oleic-acid-coated superparamagnetic iron oxide (SPIO) nanoparticles (d = 10 nm) were purchased from Ocean Nano Tech, Inc. (Arkansas, USA). Perfluoropentane (PFP, boiling point of 29 °C), fluorescence dyes (1,1'-dioctadecyl-3,3,3',3' tetramethylindocarbocyanine perchlorate

(DiI), 3,3'-dioctadecyloxacarbocyanine perchlorate (DIO) and 1,1'-dioctadecyl-3,3,3',3'-tetramethylindo-tricarbocyanine iodide (DIR)) were obtained from Sigma–Aldrich (St. Louis, MO, USA). Herceptin was purchased from F. Hoffmann-La Roche. Cell Counting Kit-8 (CCK-8) was obtained from Dojindo Molecular Technologies (China). All chemicals used in this work were of analytical grade and were used as received.

Preparation of nanoparticles

The particles were fabricated using a double emulsion (water/oil/water) process. After Chloroform (CHCl$_3$) was added to dissolve PLGA-PEG$_{10,000}$ (10 mg), the SPIO nanoparticles (60 μL, 25 mg·mL^{-1}) and DIR (0.1 mg) were added to the PLGA solution. The mixture was emulsified using an ultrasonic probe (Sonics & Materials, Inc., USA) after adding PFP (200 μL) to the solution for the first emulsion. The above emulsified solution was poured into PVA solution and homogenized within 5 min for the second emulsion. The final emulsion was mixed magnetically for 6 h to extract the CHCl$_3$. The solution was then centrifuged at 13610 × g for 3 min and washed with deionized water three times. All processes were under ice bath. Finally, the sediment was collected and stored at 4 °C for further use.

Herceptin conjugation

Conjugation of Herceptin (HER) to the PEGylated nanoparticles was performed according to the Carbodiimides method. Briefly, DIR-SPIO-PLGA/PFP nanoparticles were dissolved in 2-(N-morpholino) ethanesulfonic acid (MES) buffer (0.1 M, pH 5.5). A mixture of 30 mg N-(3-dimethyl-aminopropyl)-N'-ethylcarbodiimide hydrochloride (EDC) and 10 mg N-hydroxysuccinimide (NHS) were added and agitated at room temperature for 1 h. After phosphate buffer solution (PBS) washing and centrifugation, the sediment was redissolved in MES buffer (0.1 M, pH 8). Then excess Herceptin was added and stirred overnight. The resulting solution was washed using PBS and the supernatant discarded. The final HER-DIR-SPIO-PLGA/PFP nanoparticles were harvested *via* centrifuge (13610 × g, 3 min) three times. The PEGylated PLGA nanoparticles encapsulating PFP (PLGA/PFP), PEGylated PLGA nanocapsules without DIR (HER-SPIO-PLGA/PFP) or SPIO (HER-DIR-PLGA/PFP) were fabricated and used as control groups.

Structural characterization of nanoparticles

The morphological and structural characterization, size distribution, and zeta potential were measured using scanning electron microscopy (SEM, JEOL JSM-7800F), transmission electron microscopy (TEM, Hitachi H-7600, Japan) and dynamic light scattering (DLS, Malvern Instruments, Malvern, UK). The optical absorption properties were assessed using a UV-vis spectrophotometer (UV-2550, SHIMADZU, Japan). The amount of SPIO nanoparticles encapsulated in the HER-DIR-SPIO-PLGA/PFP was measured using inductively coupled plasma optical emission spectrometry (ICP-OES). To assess the connection ratio of the HER-DIR-SPIO-PLGA/PFP, a secondary antibody labeled by FITC was combined with the HER-DIR-SPIO-PLGA/PFP or DIR-SPIO-PLGA/PFP and viewed using confocal laser scanning microscopy (CLSM, Nikon A1, Japan) and flow cytometry analysis (FACSVantage, Becton, Dickinson and Company, USA).

In vitro photothermal effect

The photothermal effects of the nanoparticles were investigated by placing 0.2 mL of various concentrations of DIR-SPIO-PLGA/PFP nanoparticles (0, 3.75, 7.5, 11.25 and 15 mg·mL^{-1}) on a 96-well plate (Nest Biotechnology Co. LTD), and then irradiated by NIR laser for 10 min (808 nm, 2 W·cm^{-2}). The heating effects of different laser energy (1, 1.5, 2 W·cm^{-2}) with DIR-SPIO-PLGA/PFP nanoparticles (11.25 mg·mL^{-1}) and different nanoparticles (DIR-SPIO-PLGA/PFP, SPIO-PLGA/PFP, DIR-PLGA/PFP and PLGA/PFP) with the same concentration (11.25 mg·mL^{-1}) were also tested. A microscope (Olympus America, Inc; Center Valley, PA) was used to record the optical images before and after irradiation. An infrared (IR) thermal imaging system (Fluke Ti32, Fluke Corporation, USA) was used to measure the temperature during irradiation.

In vitro MR/PA/US imaging

For MR imaging, nanoparticles were mixed with 1% agar solution to create SPIO concentrations of 0.0431, 0.0862, 0.1724, 0.2586, 0.3448 mM. Once the mixture was fully dissolved, samples were transferred into eppendorf tubes 1 cm in diameter and allowed to set. MRI samples were imaged using a Philips 3.0 T MRI scanner. With scanning sequence for fast field echo FFE (TR = 500, TE = 23, flip 18°, FOV = 180 mm, slice thickness = 3.0 mm), then T2*-weighted images (T2*WI) were obtained. The T2* values within the regions of interest (ROI) were measured.

Photoacoustic imaging of the nanoparticles was performed by scanning the excitation wavelength of the photoacoustic imaging system (Vevo LAZR, Canada) from 680 to 970 nm. Photoacoustic signals of various concentrations of nanoparticles (SPIO concentration: 0.0862, 0.1724, 0.2586, 0.3448, 0.431

mM) were measured using 754 nm.

To examine the vaporization process, the nanoparticles (0.8 mg·mL^{-1}) in gel phantoms (2% agar w/v in distilled water) were irradiated using an 808 nm laser (FC-808-2W-MM, Mid-River, Xian, China) at a power density of 2 W·cm^{-2}. After laser irradiation, the samples were scanned using an ultrasonic diagnostic instrument (Mylab 90, Esaote, Italy) in conventional B-mode and contrast-enhanced ultrasound mode (CEUS) using a LA523 linear probe. PLGA/PFP and saline were used as controls. The echo intensities within the ROI were measured.

Cell experiments

The breast cancer cell lines SKBR3 (HER2 receptor positive) and MDA-MB-231 cells (HER2 receptor negative) were obtained from Medicine Laboratory of the Third Military Medical University. SKBR3 cells and MDA-MB-231 cells were cultured in McCoy's 5A modified medium and BPMI-1640 medium respectively, supplemented with 10% fetal bovine serum and 1% penicillin–streptomycin. The cell lines were incubated at 37 °C with 5% CO_2.

For the *in vitro* cytotoxicity test, SKBR3 cells and MDA-MB-231 cells were cultured with HER2 targeted nanoparticles and controls. Cells (1 × 10^4 cells per well, 100 µL) were seeded into 96-well plates and incubated for 24 h. The old medium was replaced with the medium containing different doses of nanoparticles (0-2 mg·mL^{-1}), or Herceptin (0-113.2 µg·mL^{-1}). Untreated cells in growth media were used as a control. After incubation for 24 h, the cell viability was evaluated by the CCK-8 assay.

For photothermal effect evaluation, different concentrations of HER2 targeted nanoparticles were added into wells containing SKBR3 cells and MDA-MB-231 cells for 2 h, with free PLGA/PFP (2 mg·mL^{-1}) and laser as control groups. The 96-well plates were washed with PBS and exposed to an 808 nm laser at a power density of 2 W·cm^{-2} for 30 s. Then, cells were transferred into fresh medium and further incubated for 2 h before the CCK-8 assay.

For *in vitro* cellular uptake study, SKBR3 and MDA-MB-231 cells were seeded into a 6-well plate at a density of 1 × 10^5 cells per well. After incubation for 24 h, the solutions were replaced with serum-free medium containing HER2 targeted nanoparticles, controls and/or free Herceptin (100 µg·mL^{-1}). The nanoparticle concentration in all 3 groups was 1 mg·mL^{-1}. After incubation for 0.5 h, the cells were washed three times with PBS and then fixed with 4% paraformaldehyde for 10 min. Then, the cells were washed with PBS again, and the nuclei were stained with DAPI (10 µg·mL^{-1}) for 10 min. The cytomembrane was labeled with DIO for 10 min. The remaining DAPI and DIO were washed off with PBS, and the fixed cells were imaged using a confocal laser scanning microscope (Nikon A1, Japan).

Animal studies

All animal experiments were approved by the Animal Ethics Committee of Chongqing Medical University. Female nude mice (4-6 weeks; 18-22 g) were purchased from and bred at the Animal Center of Chongqing Medical University. To establish the tumor model of nude mice, SKBR3 cells were suspended in serum-free McCoy's 5A modified medium (1 × 10^6 cells per mouse) and administered subcutaneously to the flanks of the mice. The experiments were initiated when the tumors reached a volume of 200 mm^3 [length × (width)^2/2].

In vivo toxicity and biodistribution studies

Healthy kunming mice were intravenously injected with HER2 targeted nanoparticles (200 µL, 15 mg·mL^{-1}) and sacrificed on the 7th, 14th, or 30th day (four mice per group) after injection. Another four healthy kunming mice were used as the controls. Before the mice were euthanatized, blood samples (~1 mL) were collected and sent to the second affiliated hospital of Chongqing Medical University for blood biochemistry testing. In the same way, to examine circulation time of nanoparticles *in vivo*, blood samples were collected for detecting DIR concentration by fluorescence spectrophotometry (Cary Eclipse Fluorescence Spectrophotometer, Agilent Technologies) at different time points post-injection (n = 3 for each time point). For biodistribution, nude mice bearing SKBR3 xenograft were injected with the above dose of targeted nanoparticles, with untreated nude mice as control. Major organs including heart, liver, spleen, lung, kidney, brain and tumor from nude mice were solubilized at prescribed time points (0.5, 6, 24 h) by aqua regia for ICP-OES to determine iron contents in various organs (n = 3 per group).

In vivo imaging

When the tumor volumes reached ~200 mm^3, the mice were classified into three groups (3 mice in each group). One group was injected with HER-DIR-SPIO-PLGA/PFP; the second group was injected with DIR-SPIO-PLGA/PFP; the third control group with saline only. All experiments were conducted under complete anesthesia using 3% isoflurane. Before the injection (200 µL of nanoparticles (concentration: 10 mg·mL^{-1})), control images of the tumor regions were acquired with MR, photoacoustic, ultrasound and NIRF imaging.

For MR imaging, nanoparticles were injected

through the tail-vein of the mouse to obtain images at 0.5, 6, and 24 h post injection using a Bruker 7.0 T MRI scanner (BIOSPEC70/20USR, German). The imaging parameters for the T2-weighted gradient-echo were TR = 3000, TE = 30, flip 90°, FOV = 4 cm, slice thickness = 1.0 mm. The T2 values within the ROI were measured. For photoacoustic imaging, nanoparticles were injected through the tail-vein of the mouse to obtain images at the same time points post injection using a Vevo LAZR with a laser energy density of 2 mJ·cm⁻² at a wavelength of 754 nm, well below the 30 mJ·cm⁻² ANSI laser safety limits. For ultrasound imaging, images were used to identify the location and margin of the tumor, and the same dose of nanoparticles or saline were injected through the tail-vein of the mouse. The tumor was irradiated for 10 min using an 808 nm laser (2 W·cm⁻²) to obtain images. For NIRF imaging, the same concentration (10 mg·mL⁻¹, 200 μL) of HER-DIR-SPIO-PLGA/PFP or DIR-SPIO-PLGA/PFP was administrated intravenously by the tail vein. At each time point, NIRF images were acquired to demonstrate the *in vivo* targeted transportation of the nanoparticles. After *in vivo* imaging, all mice were sacrificed, fluorescence images of the *ex vivo* major organs including heart, liver, spleen, lung, kidney, brain and tumor were also acquired. A vital fluorescence imaging system (Xenogen IVIS Spectrum, Perkin Elmer, USA) was employed during the study. All fluorescence images were analyzed using Living Image 5.0 software.

In vivo photothermal ablation

15 tumor-bearing mice were randomly subdivided into five groups (n = 3 per group): HER-DIR-SPIO-PLGA/PFP + NIR, DIR-SPIO-PLGA/PFP + NIR, HER-DIR-PLGA/PFP + NIR, Saline + NIR, HER-DIR-SPIO-PLGA/PFP. In all groups, the mice received tail-vein injection of 200 μL nanoparticles (NPs) or saline (NPs concentration was 15 mg·mL⁻¹) and irradiated with an 808 nm laser for 10 min at 2 W·cm⁻². The laser spot was adjusted to cover the entire tumor area. An IR thermal imaging system (Fluke Ti32, Fluke Corporation, USA) was used to monitor the temperature changes of the tumor site.

Histopathological analysis

Two days after the laser irradiation, tumor tissues were harvested from the mice for microscopic examination. All harvested tissues were fixed in 4% paraformaldehyde, processed into paraffin and sectioned. Hematoxylin and eosin (H&E) staining, proliferating cell nuclear antigen (PCNA) and apoptosis expression (TUNEL) were carried out to assess tumor cell proliferation and apoptosis. The proliferation index (PI) of PCNA and the apoptotic index (AI) of TUNEL, expressed as the ratio of positively stained tumor cells to all cells, were obtained by counting the number of cells stained positively from at least 5 randomly selected high power (×400 magnification) fields by blinded observers.

To examine the penetration of nanoparticles, nine mice were randomly divided into three groups: 1) HER-DIR-SPIO-PLGA/PFP + NIR, 2) HER-DIR-SPIO-PLGA/PFP without NIR, 3) HER-DIR-SPIO-PLGA + NIR. Then, 200 μL DiI-labeled nanoparticles (concentration: 10 mg·mL⁻¹) were injected through the tail-vein of the mice. After 6 h, the tumor tissues were irradiated for 10 min using an 808 nm laser (2 W·cm⁻²). The mice were euthanized and the tumors were fixed and sectioned for histological analysis. FITC-conjugated anti-CD31 (abacom) was used to label vasculature endothelial cells. CLSM images were obtained and signal intensities were calculated using ImageJ software.

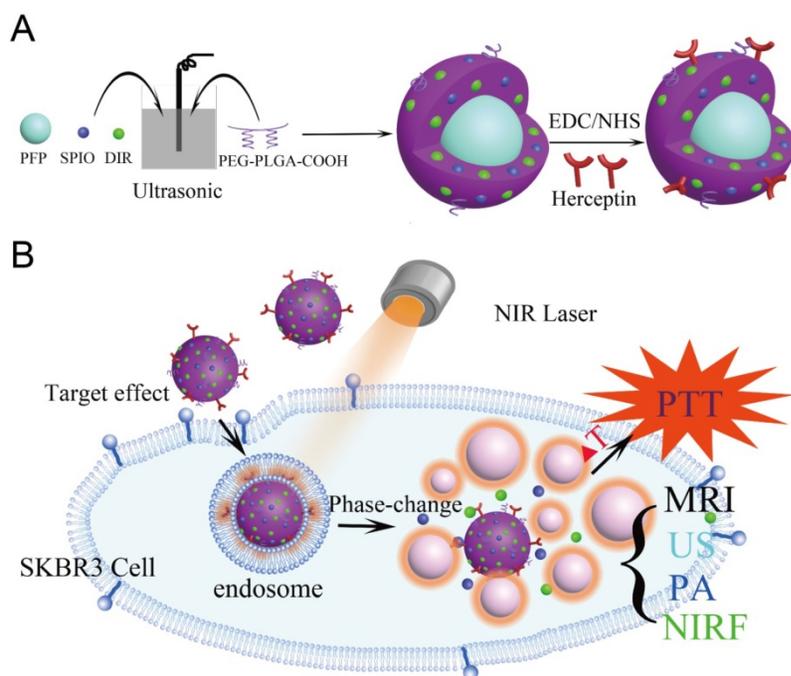## Results

Particle characterization

The nanoparticles were synthesized using a modified double emulsion evaporation process, where SPIO, DIR and PFP were introduced into the reaction medium in different steps (Figure 1). The nanoparticles exhibited a well-defined spherical morphology with SPIO evenly distributed in the shell (Figure 2A, B). The nanoparticle average diameter without Herceptin was 278 nm and the Herceptin coating increased the diameter to 298 nm (Figure 2C). The zeta potential with and without Herceptin was similar at -1.78 mV and -2.61 mV, respectively (Figure S1). The absorption spectrum of the nanoparticle constituents is shown in Figure 2D, where a slight absorption peak at 764 nm in the NIR region was observed. The temperature increase of the nanoparticles in water when irradiated by a NIR laser (808 nm, 2W·cm⁻²) is shown in Figure 2E, where a steady temperature of 60 °C (at 3.75 mg·mL⁻¹) up to nearly 90 °C (at 15 mg·mL⁻¹) was achieved over 10 min. As shown in Figure 2F, nanoparticles without SPIO only achieved 43.7 °C, while the temperature of DIR-SPIO-PLGA/PFP and SPIO-PLGA/PFP nanoparticles (NPs concentration: 11.25 mg·mL⁻¹) reached up to 79.9 °C and 75.6 °C, respectively. This result verified that the main photothermal effect was contributed by SPIO. The heating effect was also dependent on the power of the incident laser (Figure S2). Following Roper's method [39], the heat conversion efficiency (η) of HER-DIR-SPIO-PLGA/PFP using 808 nm was calculated to be 5.9%. The

detailed calculations can be found in Supporting Information and Figure S3. This is less than other photothermal agents such as Au nanoshells (13%), Au nanorods (21%), Cu2-xSe nanocrystals (22%), and Graphene Oxide (25%) [40, 41]. However our nanoparticles are biocompatible with excellent imaging capabilities.

The SPIO nanoparticles had a 93% incorporation rate into the shell (measured *via* ICP-OES), while 99% of the Herceptin was bound to the shell (measured *via* flow cytometry, and confocal laser scanning microscopy) (Figure S4 and S5). Bicinchoninic acid (BCA) curve of Herceptin further demonstrated that Herceptin was highly linked with 0.28 mg·mL^{-1} (Figure S6). All the materials used in this study showed high encapsulation and loading rates. The nanoparticles were stable at 37 °C (Figure 2G), and irradiation with a near-IR laser induced vaporization (Figure 2H, I). To further evaluate their long-term stability, the targeted and non-targeted nanoparticles were stored at 4 °C in distilled water for 1 week; as a result, the sizes of the nanoparticles did not change remarkably (Figure S7), demonstrating their excellent stability.

In vitro imaging assessment in phantoms

We evaluated the multimodal imaging capabilities of the nanoparticles *in vitro* using agar-based phantoms. The intrinsic magnetic ability of the nanoparticles was examined using T2-weighted MR imaging on a 3.0 T MR scanner. The transverse relaxation time can be shortened by the SPIO nanoparticles. The nanoparticles demonstrated a linear dependency of the 1/T2* values on SPIO concentration (Figure 3A), with the transverse relaxivity (r^2) measured to be 92.73 mM^{-1}·s^{-1}, which was ~2-fold higher than the free SPIO nanoparticles [42]. Then the PA signals of the nanoparticles were also investigated. As shown in Figure S8, the photoacoustic signal of the nanoparticles was strongest at the beginning of irradiation, and then decreased to a steady state value. Evaluation using different concentrations of nanoparticles showed that the PA signal intensity increased linearly with the SPIO and DIR concentrations using 754 nm for excitation, where maximum PA absorbance occurs (Figure 3B and Figure S9). Finally, ultrasound imaging was assessed by comparing the nanoparticle performance to two controls: nanoparticles without DIR and SPIO (designated PLGA/PFP), and saline before and after irradiation. No difference in the image contrast was observed using B-mode and CEUS for the two controls before and after irradiation. However, in the experimental group, the B-mode and CEUS image contrast increased by 4.7 times and 136 times respectively (Figure 3C, D). These quantitative results further demonstrate the requirement of the SPIO/DIR optically absorbing components for facilitating the PFP vaporization process, and the sensitivity that ultrasound can detect and verify that vaporization occurred. The enhanced ultrasound contrast due to microbubble formation persisted for more than 1 h, as shown in Figure S10. These results demonstrate the feasibility of using the nanoparticles in multimodal imaging.

Targeting performance and cytotoxicity in cells

The targeting performance and cytotoxicity of the nanoparticles were examined in cell culture using SKBR3 (over-expressing HER2) and MDA-MB-231 (HER2 negative) cells. The HER2 targeted nanoparticles were incubated with cells for 30 min, and compared to two controls: HER2 targeted nanoparticles with free Herceptin (to block the HER2

Figure 1. (A) The preparation process of the HER2 targeted nanoparticles. (B) These nanoparticles are smart multifunctional theranostic agents used for MRI/US/PA/NIRF diagnostic imaging and photothermal tumor ablation. HER2 targeting ligands ensure attachment to HER2 expressing tumor cells. Upon laser irradiation at the tumor site, the liquid PFP core in the nanoparticle vaporizes and converts into microbubbles. The violent vaporization process destroys tumor tissue, and expels the SPIO and DIR nanoagents into the tumor for effective photothermal therapy.

receptors on the cell membrane), and non-targeted nanoparticles. All nanoparticles were labeled with DiI to observe the uptake within the cells using CLSM. A large number of the HER2 targeted nanoparticles were attached to the SKBR3 cells as observed through strong DiI fluorescence, while there was weak fluorescence from the MDA-MB-231 cells, indicating poor attachment (Figure 4A). Figure 4B showed the fluorescence of a single SKBR3 cell incubated with HER2 targeted nanoparticles. The two controls showed similarly poor uptake by both cell types, demonstrating the strong targeting ability of the HER2 targeted nanoparticles towards HER2 positive cells.

Cytotoxicity evaluation of the nanoparticles was then assessed using CCK-8 viability assay. Co-incubation with MDA-MB-231 cell lines for 24 h showed negligible cytotoxicity using free Herceptin, HER2 targeted and untargeted nanoparticle concentrations up to 2 mg mL^{-1} (Figure 4C). When incubated with SKBR3 cells, the non-targeted nanoparticles showed negligible cytotoxicity; however, the HER2 targeted nanoparticles showed a 5-15% decrease in cell viability (Figure 4D, black and red bars). This is likely due to the ligand, which blocks HER2 cleavage and inhibits HER2-positive breast cancers [43]. To demonstrate the PTT effect of targeted nanoparticles against the specific cell lines, the SKBR3 and MDA-MB-231 cells were incubated with HER2 targeted nanoparticles for 0.5 h and then irradiated with a laser (808 nm, 2 W cm^{-2}) for 30 s. The MDA cells showed no change in cell viability after irradiation, while the SKBR3 cells showed a decrease in viability with increasing nanoparticle concentrations (Figure 4E). This demonstrates the affinity of the HER2 targeted nanoparticles for HER2 expressing cells, and results in selective cell kill using photothermal therapy.

In vivo toxicity and biodistribution studies

We then quantified the biodistribution and the possible metabolic pathway of the iron in the nude mice, where retention and accumulation of SPIO nanoparticles in the internal organs can cause safety issues [44]. The blood retention time of the nanoparticles was up to 24 h (Figure S11), with PEG significantly increasing circulation time compared to nanoparticles without PEG [45]. Numerous studies have shown slow iron excretion [46, 47]. The biodistribution of iron in the heart, liver, spleen, lung, kidney, brain and tumor were analyzed before injection and at 0.5, 6 and 24 h after intravenous injection (Figure S12). In all organs, accumulation peaked at 6 h post injection, and levels returned to 0.5 h levels after just 24 h. Iron accumulation in the lungs was particularly high at 6 h. H&E staining of the major organs at day 21 post administration further observed no pathological damage to major organs at the studied doses, reflecting the nanoparticle non-
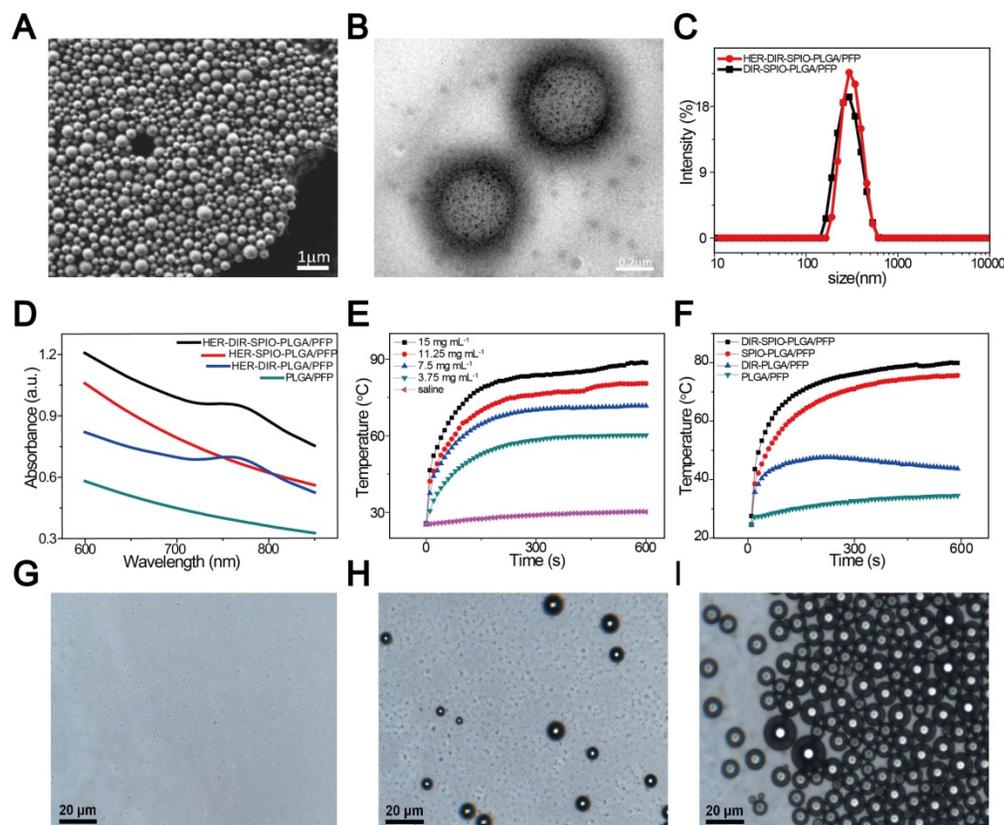
Figure 2. Particle characterization. (A) A SEM image of the HER2 targeted nanoparticles. (B) The TEM image shows the location of the SPIO nanoparticles within the PLGA shell (black dots). (C) Size distribution of HER2 targeted (red) and untargeted (black) nanoparticles in aqueous solution measured by dynamic light scattering (DLS). (D) UV-vis spectra of the nanoparticles and their constituents. (E) Temperature elevation of different concentrations of DIR-SPIO-PLGA/PFP nanoparticles within 10 min irradiation time. (F) Photothermal curves of different nanoparticles irradiated at 2 W cm^{-2} for 10 min. Optical microscopy images of the nanoparticles before (G), 20 s (H) and 1 min (I) after laser irradiation.

toxicity (Figure S13). Blood and liver biochemical markers demonstrated no significant differences between mice injected with nanoparticles, and mice without (Figure S14). These results demonstrate that these nanoparticles are *in vivo* biocompatible and non-toxic nanotheranostic agents for cancer treatment.

### In vivo targeting and imaging performance

We then tested the multimodal imaging properties of the nanoparticles *in vivo* using a SKBR3 breast xenograft model in nude mice. In accordance with the Animal Ethics Committee of Chongqing Medical University, 1×10^6 SKBR3 cells were administered subcutaneously to the flanks of female mice from the Experimental Animal Center of Chongqing Medical University. Once the tumor volumes reached 200 mm³, the mice were injected *via* tail vein with either HER2 targeted nanoparticles, untargeted nanoparticles (control 1), or saline (control 2). All experiments were performed under complete anesthesia using 3% isoflurane. MR and PA imaging were performed at pre-injection, and 0.5, 6 and 24 h post injection. MRI measurements were made using a Bruker BIOSPEC70/20USR 7.0 T MRI scanner. The

1/T2 signal from the tumor site peaked at 6 h post injection using HER2 targeted nanoparticles; this effect was evident in the T2 weighted images, where the tumor region became darker over time (Figure 5A, B). No changes were observed using the two controls. The SPIO component of the nanoparticles strongly absorbs in the near-IR region, enabling their use in PA imaging. A Visualsonics Vevo LAZR was used to acquire PA images using a 21 MHz transducer and 754 nm laser wavelength. The PA signal using the targeted nanoparticles increased by 74% at 6 h post injection (Figure 5C, D), which was consistent with the MRI results. The non-targeted nanoparticles showed a slight increase in PA signal at 0.5 h, which stabilized at 6 h, then decreased. The saline group showed a decrease in signal over all time points.

US imaging provides real time anatomical imaging such as the tumor boundaries, but also indicates if vaporization of the nanoparticles occurred through increased contrast due to the high echogenicity of the microbubbles. B-mode imaging and CEUS were performed on the tumors using a Mylab 90 ultrasound system at 5-12 MHz frequency, before and after irradiation with an 808 nm laser for 10 min. B-mode imaging enabled clear quantification of the tumor volume and periphery, while CEUS indicated 12-fold increased contrast around the tumor for the HER2 targeted nanoparticles compared to the controls (Figure 5E, F).

We then used NIRF imaging to track the *in vivo* delivery and biodistribution of the nanoparticles (Figure 5G, H). Significant fluorescence signal accumulated in the tumor in the targeted group and peaked at 6 h, which was 3.4-fold higher compared to the non-targeted group $((1.18 \pm 0.33) \times 10^8$ vs $(3.47 \pm 0.65) \times 10^7$ $(p \cdot s^{-1} \cdot cm^{-2} \cdot sr^{-1})/(\mu W \cdot$
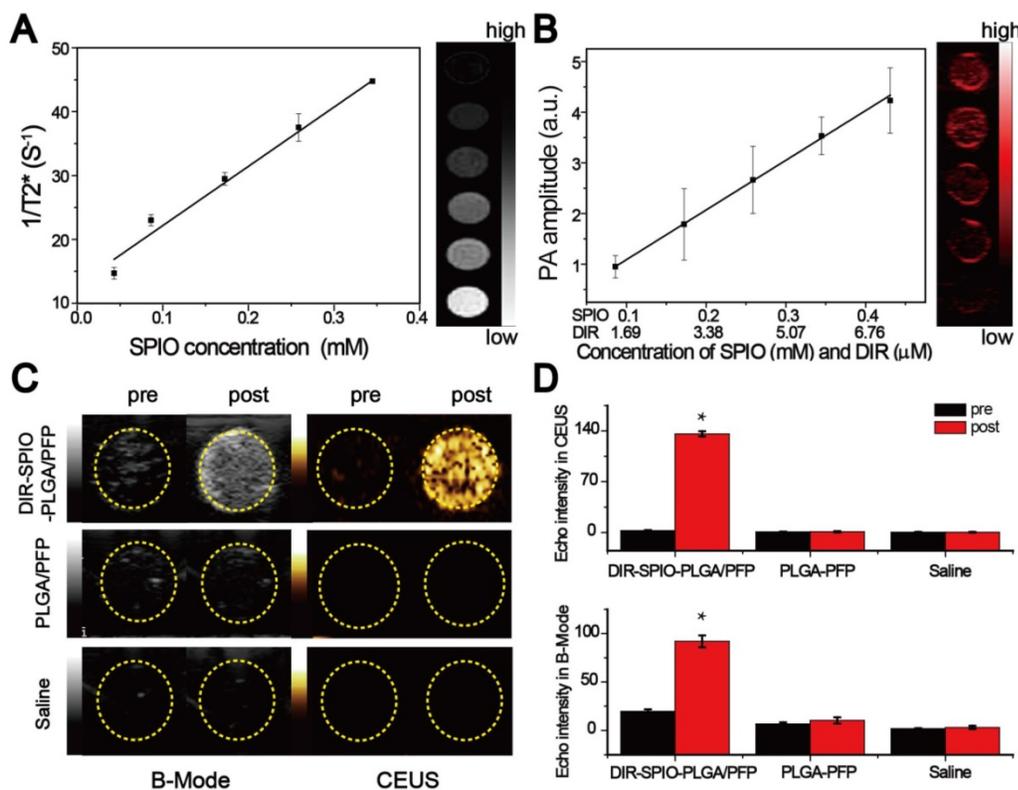

Figure 3. In vitro imaging. (A) T2* relaxation rate ($1/T2^*(s^{-1})$) of the nanoparticles at different SPIO concentrations in agarose gel. The colorbar indicates the T2*-weighted MRI image. (B) Measured photoacoustic amplitude of the nanoparticles at various concentrations. (C) B-Mode and contrast enhanced ultrasound (CEUS) imaging of the nanoparticles before and after laser irradiation *in vitro* using gel phantoms for the nanoparticles compared to two controls: nanoparticles without SPIO and DIR (middle row), and saline only (bottom row). (D) Echo intensity (EI) of the CEUS and B-Mode before and after laser irradiation. (*P < 0.05)

cm^{-2}) respectively). After 24 h, *ex vivo* fluorescence images of the excised major organs showed that the nanoparticles accumulated in the reticuloendothelial system. Moreover, fluorescence intensity of the tumor in the targeted group was still 1.5-fold greater compared with the non-targeted nanoparticles ((5.81 ± 1.04) × 10^7 vs (3.83 ± 0.65) × 10^7 (p·s^{-1}·cm^{-2}·sr^{-1})/(μW·cm^{-2}) respectively), further confirming the targeting capacity of our targeted nanoparticles to HER2 positive tumor tissue (Figure 5I, J).

Treatment using photothermal therapy

After demonstrating that these smart laser-activated nanoparticles can be accurately used for MR/PA/US/NIRF multimodality diagnostic imaging of HER2 positive breast cancer, we then conducted *in vivo* photothermal therapy tests using the SKBR3 xenograft nude mice model. The HER2 targeted nanoparticles (denoted HER-DIR-SPIO-PLGA/PFP) were compared against three controls: untargeted nanoparticles (DIR-SPIO-PLGA/PFP), targeted nanoparticles without SPIO (HER-DIR-PLGA/PFP), and saline via tail-vein injection. All procedures were performed at 6 h post injection, where maximal accumulation within the tumor was observed, as shown in Figure 5. The tumor region was irradiated for 10 min (808 nm, 2 W·cm^{-2}), and an IR thermal camera was used to monitor the temperature changes over time (Figure 6A, B). During NIR irradiation, the temperature in the tumors increased to nearly 55 °C (the thermal ablation temperature of tumor cells [48, 49]) using HER-DIR-SPIO-PLGA/PFP, which was higher than the three controls. The DIR-SPIO-PLGA/PFP increased to 47 °C, while the saline and HER-DIR-PLGA/PFP increased to 42 °C.
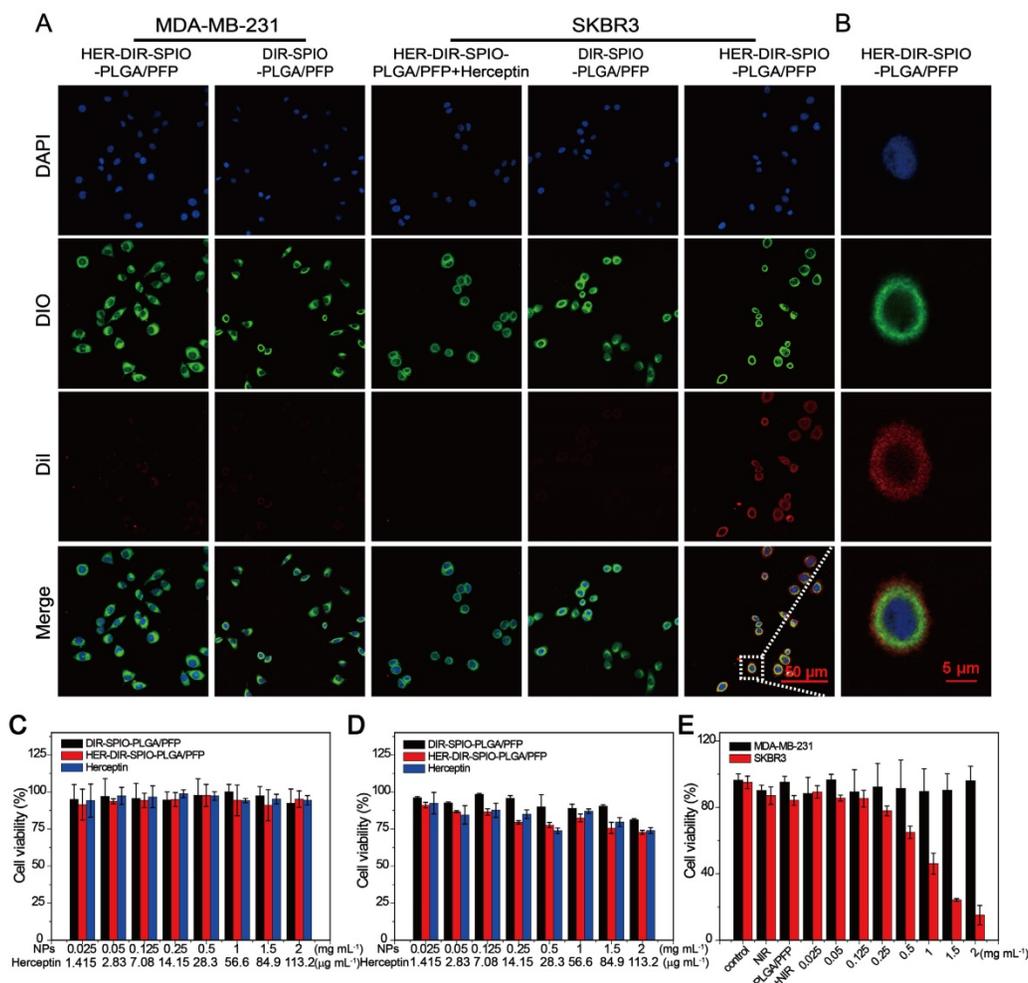
Figure 4. Targeting performance and cytotoxicity in cells. (A) Confocal laser scanning microscopy of MDA-MB-231 cells incubated with HER2 targeted nanoparticles (1st column) and untargeted nanoparticles (2nd column), SKBR3 cells incubated with HER2 targeted nanoparticles with free Herceptin (3rd column), HER2 untargeted nanoparticles (4th column) and targeted nanoparticles (5th column). From top to bottom are the DAPI labeled nuclei, DIO labeled cytolemma, DiI labeled nanoparticles and their overlay (scale bar is 50 μm). (B) Confocal laser scanning microscopy of a single SKBR3 cell incubated with HER2 targeted nanoparticles (scale bar is 5 μm). Cytotoxicity assay of (C) MDA-MB-231 cells and (D) SKBR3 cancer cells in the presence of HER2 targeted or untargeted nanoparticles or free Herceptin. (E) Photothermal effect of HER2 targeted nanoparticles with laser irradiation (808 nm laser for 30 s at power density of 2 W·cm^{-2}) at various concentrations, both in MDA-MB-231 cells and SKBR3 cells, with free laser and PLGA/PFP (2 mg mL^{-1}) as control groups.
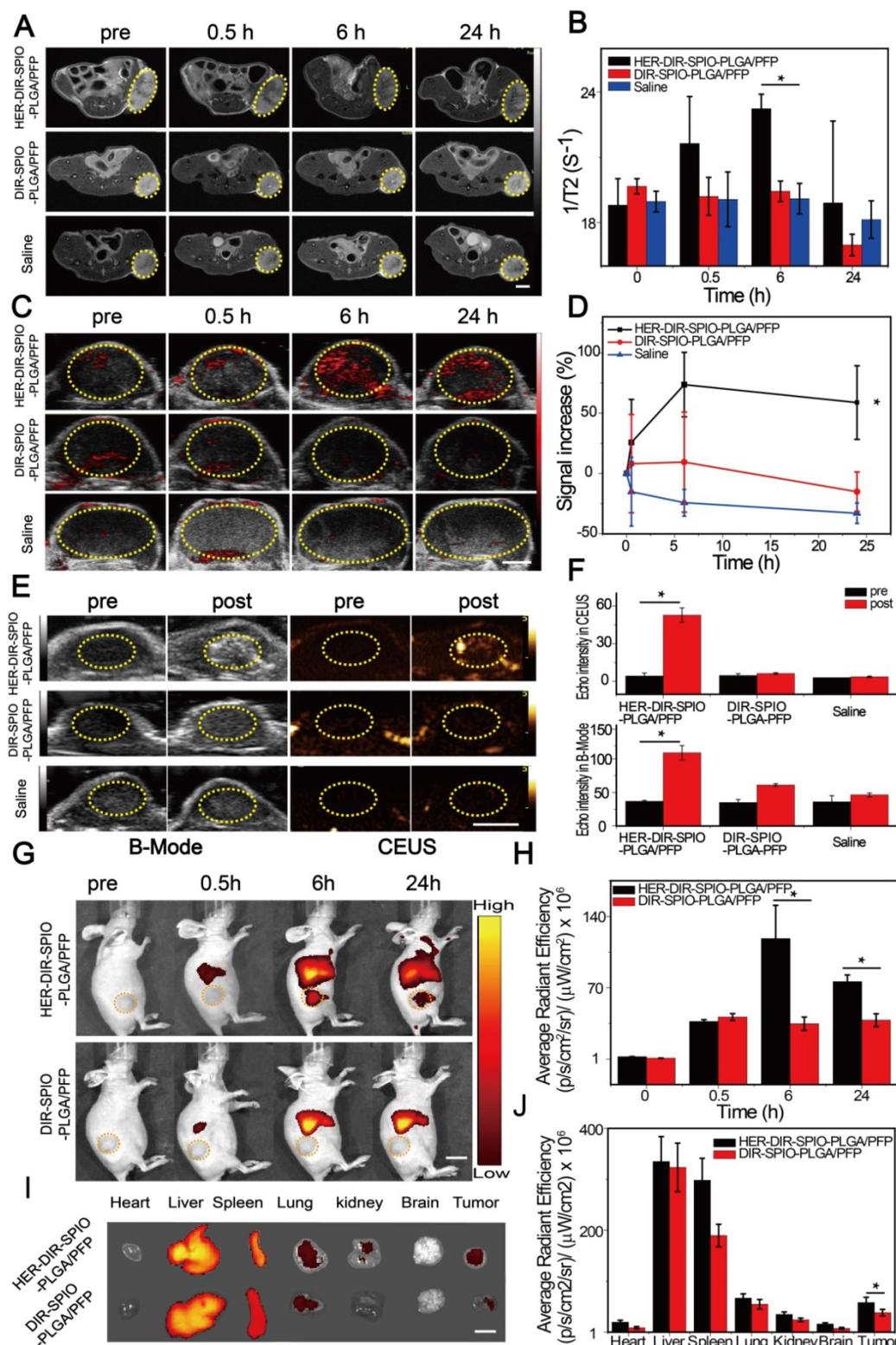
Figure 5. *In vivo* multimodality imaging performance. (A) MR images and (B) T2 relaxation rate (1/T2 (s⁻¹)) of a SKBR3 mouse xenograft tumor (yellow dashed circles) at different times after intravenous injection of the HER2 targeted nanoparticles and various controls. Scale bar = 5 mm. (C) PA images and (D) the signal increase (%) of the SKBR3 tumor (yellow dashed circles) at different times after intravenous injection of the HER2 targeted nanoparticles and various controls. Scale bar = 3 mm. (E) B-Mode and contrast enhanced ultrasound (CEUS) imaging and (F) the echo intensities of the tumor before and after laser irradiation for the HER2 targeted nanoparticles and the controls. Scale bar = 5 mm. (G) Near-infrared fluorescence (NIRF) images and (H) their average radiant efficiencies (p ·s⁻¹ ·cm⁻² ·sr⁻¹)/ (mW ·cm⁻²) of mice at different times after injection of HER2 targeted or untargeted nanoparticles. Scale bar = 1 cm. (I) The *ex vivo* fluorescence images and (J) the average radiant efficiencies (p ·s⁻¹ ·cm⁻² ·sr⁻¹)/ (mW ·cm⁻²) of the HER2 targeted and untargeted nanoparticles in various tissues after 24 h. Scale bar = 1 cm. Data are given as the mean ± standard deviation (SD), n = 3, *P < 0.05.
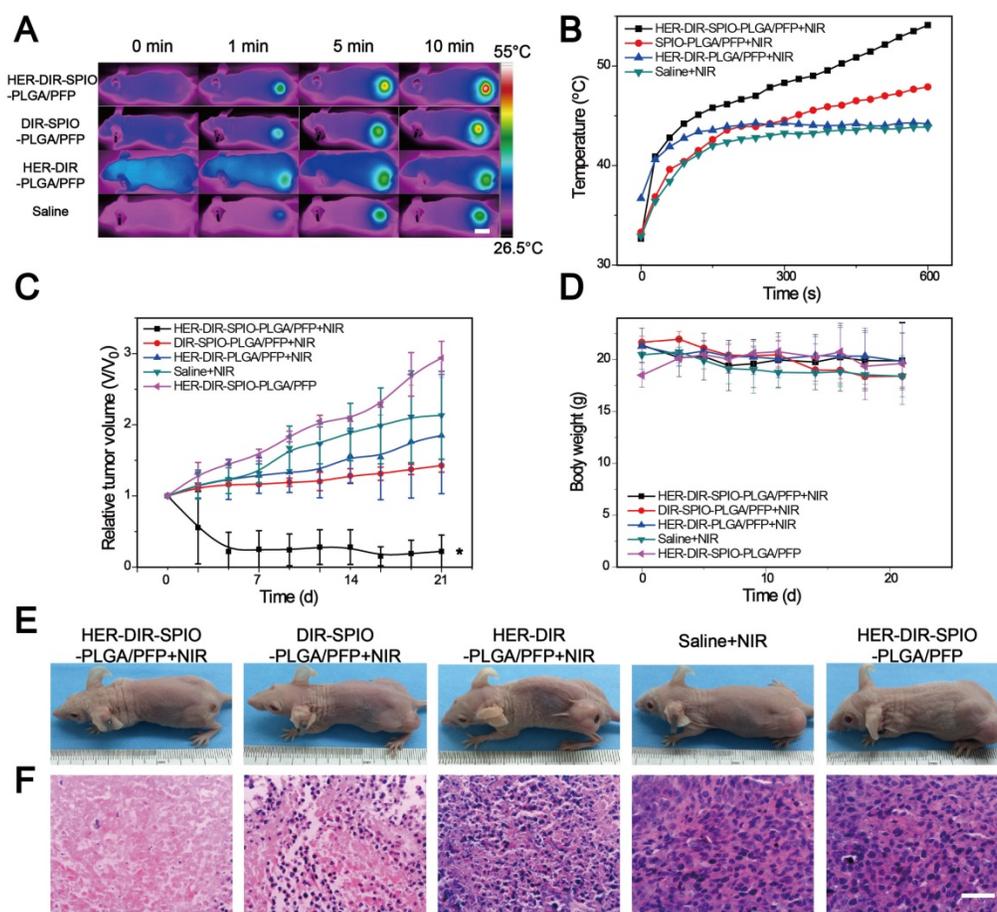
Figure 6. *In vivo* thermal imaging, photothermal therapy. (A) IR thermal images of treatment groups and (B) temperature variation of tumor-bearing mice after intravenous injection of the HER2 targeted nanoparticles and controls and irradiation for 10 min using an 808 nm laser at 2 W cm^{-2} (6 h post injection, mean ± SD, n = 3, scale bar = 1 cm). (C) The relative tumor growth curves and (D) mice body weights during the various treatments over the 21 day study period (mean ± SD, n = 3, *P < 0.05). (E) Representative photos of mice bearing SKBR3 tumor with different treatments after 21 days. (F) Microscopy images of H&E stained tumor tissues in various groups (×400 magnification, scale bar = 100 μm).

Finally, we investigated how PTT affects tumor growth over 21 days. The HER2 targeted nanoparticles were compared against the three controls as above, and HER2 targeted nanoparticles without PTT as another control. A total of 15 mice were examined, three per group. The PTT treatment was performed at day 0, and the relative tumor volume (determined *via* US, Figure 6C) and body weight (Figure 6D) was measured every 2-3 days for 21 days. In the control HER-DIR-SPIO-PLGA/PFP group without laser irradiation, tumor volume increased rapidly ~3-fold. The saline and HER-DIR-PLGA/PFP groups showed similar increases in tumor volume of 2.13-fold and 1.85-fold, respectively. The DIR-SPIO-PLGA/PFP group was slightly more effective at controlling tumor volume, with a tumor volume increase of 1.43-fold. The mice with HER2 targeted nanoparticles with irradiation showed a remarkable response to treatment, with the tumors rapidly shrinking at just day 3, and one tumor disappeared completely (Figure 6C, E). The body weight of mice for all five groups did not change significantly during the period of observation (Figure 6D), indicating that the mice did not have an acute toxicity response.

Treatment effectiveness was evaluated using H&E stained tumor slices (Figure 6F) and immune-histochemical staining against PCNA and TUNEL assays (Figure S15). The H&E slices in the HER-DIR-SPIO-PLGA/PFP group were largely representative of normal tissue with normal morphology. The controls showed varying degrees of irregular cell size and shape, indicative of tumor tissue. Our results indicated that proliferative cells (brown nucleus) were observed in all groups, and the PI of tumor in the group of HER-DIR-SPIO-PLGA/PFP combined laser was significantly lower than those for any other group (*p < 0.05). Similar to the TUNEL expression, the AI of the tumor in the group of HER-DIR-SPIO-PLGA/PFP + NIR was also higher than those for the other groups (*p < 0.05).

Next, we examined the tumor penetration ability of the nanoparticles after systemic administration in a SKBR3 xenograft nude mouse model (Figure 7). In the

nanoparticle plus NIR irradiation group, large numbers of blood vessels were destroyed, resulting in deeper penetration of the nanoparticle fragments within the tumor. In contrast, without NIR irradiation, nanoparticle signals (red) were localized near vascular areas, resulting in a shallower penetration depth than that of the NIR group. To further verify that the vasculature destruction was due to nanoparticle vaporization rather than the PTT effect, nanoparticles (without PFP) plus laser irradiation was also evaluated. Fewer blood vessels were destroyed without PFP and the nanoparticles were localized closer to the vessels as compared to the nanoparticle plus NIR group. This difference demonstrates that PFC nanoparticles can be utilized to improve tumor penetration via laser-activated vasculature destruction.

Discussion and Conclusions

There is a need for accurate targeting of HER2 positive tumors for diagnostic imaging and therapy. Nano-based medicine is poised to make a breakthrough in the treatment of cancer [50-52]. To meet this demand, we developed targeted theranostic nanoparticles for combined diagnostic imaging and therapy of HER2 expressing breast cancer. As the size of the nanoparticles decreases, the Laplace pressure increases, increasing the PFP boiling point inside the nanoparticle [25]. The hard shell prevents spontaneous evaporation that can occur with soft-shelled PFP-based nanoparticles. During laser irradiation, SPIO and DIR absorb the laser energy, creating heat, resulting in the phase transition. The combination of these components in a nanoscale particle enable multimodal imaging through MRI, PA, NIRF, and US, which are emerging imaging platforms with promise for cancer-related diagnoses.

A common problem with nanoparticle-based medicines is rapid clearance rates, with a half-life of hours [53, 54]. The PEG coating significantly improves circulation times [55, 56], while the HER2 ligands promote nanoparticle retention at the tumor site. These combined effects show a peak accumulation within the tumor at 6 h post injection, maintaining significant retention at 24 h (Figure 5). Cellular toxicity is minimal, with significant cell death occurring only in HER2 expressing cells during PTT. The nanoparticles exhibited good biocompatibility, with no adverse effects observed during the 21 day animal studies where liver function and body weight were normal.
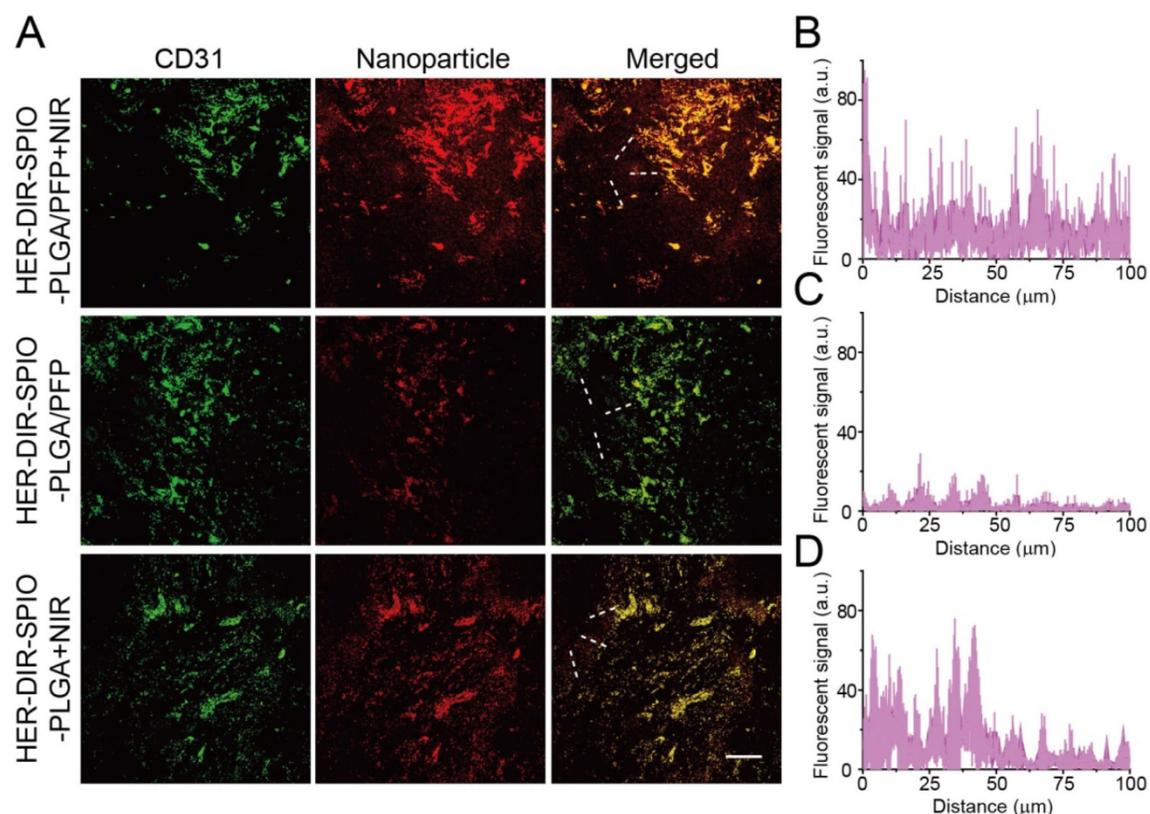
Figure 7. (A) Representative confocal microscopy images of nanoparticle distribution in histological sections from the tumors administered with either DiI-labeled nanoparticles + NIR (top row), nanoparticles without NIR (middle row) or nanoparticles without PFP + NIR (bottom row) (green: tumor vasculature, red: nanoparticles; scale bar = 100 μm). (B-D) The relative fluorescent signal of nanoparticles from the vasculature towards the tumor center indicated by the white dashed lines on the merged images in (A) (n = 3; mean ± SD).

Most nanoparticle based therapies rely on the EPR effect to diffuse into the tumor regions and deliver a payload. Questions remain whether the EPR effect alone is sufficient for improving response and survival of cancers [57]. Nanoparticle delivery to tumors is hindered by poor uptake [58, 59], and nanoparticles are generally found <100 μm from vessels [60, 61]. Also, specific targeting ligands do not enhance intratumoral penetration [62]. While a proportion of our nanoparticles are small enough to pass through the leaky vasculature, the vaporization process aids in distributing the nanoparticles and its constituents throughout the tumor. Upon laser irradiation, the nanoparticles are activated and violently vaporize. The vasculature surrounding the nanoparticles is destroyed, enabling further penetration of the nanoparticle fragments into the tumor. As the area is continually irradiated, more nanoparticles are vaporized, creating a cascading effect of tumor destruction and deeper penetration. Combining laser and ultrasound irradiation can also be used to facilitate PFC droplet vaporization, enhancing the tissue penetration of the nanoparticles [63-65]. The therapeutic effects of PTT here are amplified due to enhanced distribution of SPIO and DIR throughout the tumor compared to existing nanomedicine therapies that rely on the EPR effect alone. Moreover, the widespread tissue damage can elicit an immune response for further killing efficacy [66]. Successive treatments over days can further enhance the effectiveness of this multi-targeted approach [22].

Many studies have shown synergistic effects through multi-modal treatment types. Future work will focus on incorporating a chemotherapeutic payload into the nanoparticle, where upon irradiation, a high drug dose can be delivered directly into the tumor site, avoiding systemic side effects commonly associated with intravenous chemotherapy. The combination of long circulation time, retention within the tumor via HER2 targeting, and synergistic therapies (physical disruption via ODV, cell death via PTT and targeted drug delivery) may improve treatment effectiveness for HER2 expressing tumors, leading to improved survival of one of the deadlier breast cancers today.

Abbreviations

PFP: perfluoropentane; PLGA: poly (lactic-co-glycolic acid); DIR: 1,1'-dioctadecyl-3,3,3',3'-tetramethylindotricarbocyanine iodide; SPIO: superparamagnetic iron oxide nanoparticles; MR: magnetic resonance; PA: photoacoustic; NIRF: near-infrared fluorescence; US: ultrasound; MRI: magnetic resonance imaging; PTT: photothermal therapy; PFC: perfluorocarbon; ODV: optical droplet vaporization; FDA: Food and Drug Administration; PEG: polyethylene glycol; NIR: near infrared; DiI: 1,1'-dioctadecyl-3,3,3',3' tetramethylindocarbocyanine perchlorate; DIO: 3,3'-dioctadecyloxacarbocyanine perchlorate; CCK-8: Cell Counting Kit-8; CHCl$_3$: Chloroform; MES: 2-(N-morpholino) ethanesulfonic acid; EDC: N-(3-dimethylaminopropyl)-N'-ethylcarbodiimide hydrochloride; NHS: N-hydroxysuccinimide; PBS: phosphate buffer solution; SEM: scanning electron microscopy; TEM: transmission electron microscopy; DLS: dynamic light scattering; UV-vis: ultraviolet visible; ICP-OES: inductively coupled plasma optical emission spectrometry; CLSM: confocal laser scanning microscopy; IR: infrared; CEUS: contrast-enhanced ultrasound mode; ROI: region of interest; ANSI: American National Standards Institute; H&E: hematoxylin and eosin staining; PCNA: proliferating cell nuclear antigen; TUNEL: apoptosis expression; PI: proliferation index; AI: apoptotic index; BCA: bicinchoninic acid; EPR: enhanced permeability and retention.

Supplementary Material

Figures S1-S15 and photothermal conversion efficiency calculation.
http://www.thno.org/v07p4410s1.pdf

Competing Interests

The authors have declared that no competing interest exists.

References

1. Chen CY, Yang CY, Chen YC, et al. Decreased expression of stomatin predicts poor prognosis in HER2-positive breast cancer. BMC cancer. 2016; 16: 697.
2. Recondo G Jr, de la Vega M, Galanternik F, et al. Novel approaches to target HER2-positive breast cancer: trastuzumab emtansine. Cancer Manag Res. 2016; 8: 57-65.
3. Gianni L, Pienkowski T, Im Y-H, et al. Efficacy and safety of neoadjuvant pertuzumab and trastuzumab in women with locally advanced, inflammatory, or early HER2-positive breast cancer (NeoSphere): a randomised multicentre, open-label, phase 2 trial. Lancet Oncol. 2012; 13: 25-32.
4. Lee CH, Dershaw DD, Kopans D, et al. Breast cancer screening with imaging: recommendations from the Society of Breast Imaging and the ACR on the use of mammography, breast MRI, breast ultrasound, and other technologies for the detection of clinically occult breast cancer. J Am Coll Radiol. 2010; 7: 18-27.
5. Bleyer A, Welch HG. Effect of three decades of screening mammography on breast-cancer incidence. N Engl J Med. 2012; 367: 1998-2005.

6. Stavros AT, Thickman D, Rapp CL, et al. Solid breast nodules use of sonography to distinguish between benign and malignant lesions. Radiology. 1995; 196: 123-34.

7. Mehrmohammadi M, Yoon SJ, Yeager D, et al. Photoacoustic Imaging for Cancer Detection and Staging. Curr Mol Imaging. 2013; 2: 89-105.

8. Kitai T, Torii M, Sugie T, et al. Photoacoustic mammography: initial clinical results. Breast Cancer. 2014; 21: 146-53.

9. Zackrisson S, van de Ven SMWY, Gambhir SS. Light in and sound out: emerging translational strategies for photoacoustic imaging. Cancer Res. 2014; 74: 979-1004.

10. Zhang N, Cai X, Gao W, et al. A Multifunctional Theranostic Nanoagent for Dual-Mode Image-Guided HIFU/Chemo- Synergistic Cancer Therapy. Theranostics. 2016; 6: 404-17.

11. Li Y, Lin TY, Luo Y, et al. A smart and versatile theranostic nanomedicine platform based on nanoporphyrin. Nat Commun. 2014; 5: 4712.

12. Jin Y, Jia C, Huang SW, et al. Multifunctional nanoparticles as coupled contrast agents. Nat Commun. 2010; 1: 41.

13. Huang XH, EI-Sayed IH, Qian W, et al. Cancer Cell Imaging and Photothermal Therapy in the Near-Infrared Region by Using Gold Nanorods. J Am Chem Soc. 2006; 128: 2115–20.

14. Song J, Yang X, Jacobson O, et al. Ultrasmall Gold Nanorod Vesicles with Enhanced Tumor Accumulation and Fast Excretion from the Body for Cancer Therapy. Adv Mater. 2015; 27: 4910-7.

15. Yang K, Hu L, Ma X, et al. Multimodal imaging guided photothermal therapy using functionalized graphene nanosheets anchored with magnetic nanoparticles. Adv Mater. 2012; 24: 1868-72.

16. Zhang S, Sun C, Zeng J, et al. Ambient Aqueous Synthesis of Ultrasmall PEGylated Cu2-x Se Nanoparticles as a Multifunctional Theranostic Agent for Multimodal Imaging Guided Photothermal Therapy of Cancer. Adv Mater. 2016; 28: 8927-36.

17. Wang J, Guo F, Yu M, et al. Rapamycin/DiR loaded lipid-polyaniline nanoparticles for dual-modal imaging guided enhanced photothermal and antiangiogenic combination therapy. J Control Release. 2016; 237: 23-34.

18. Yao C, Wang P, Li X, et al. Near-Infrared-Triggered Azobenzene-Liposome/ Upconversion Nanoparticle Hybrid Vesicles for Remotely Controlled Drug Delivery to Overcome Cancer Multidrug Resistance. Adv Mater. 2016; 28: 9341-48.

19. Yang W, Guo W, Le W, et al. Albumin-Bioinspired Gd:CuS Nanotheranostic Agent for In Vivo Photoacoustic/Magnetic Resonance Imaging-Guided Tumor-Targeted Photothermal Therapy. ACS Nano. 2016; 10: 10245-57.

20. Wang Z, Huang P, Jacobson O, et al. Biomineralization-Inspired Synthesis of Copper Sulfide-Ferritin Nanocages as Cancer Theranostics. ACS Nano. 2016; 10: 3453-60.

21. Wang Y, Yang T, Ke H, et al. Smart Albumin-Biomineralized Nanocomposites for Multimodal Imaging and Photothermal Tumor Ablation. Adv Mater. 2015; 27: 3874-82.

22. Sun Y, Wang Y, Niu C, et al. Laser-Activatible PLGA Microparticles for Image-Guided Cancer Therapy In Vivo. Adv Funct Mater. 2014; 24: 7674-80.

23. Niu C, Wang L, Wang Z, et al. Laser irradiated fluorescent perfluorocarbon microparticles in 2-D and 3-D breast cancer cell models. Sci Rep. 2017; 7: 43408.

24. Strohm E, Rui M, Gorelikov I, et al. Vaporization of perfluorocarbon droplets using optical irradiation. Biomed Opt Express. 2011; 2: 1432–42.

25. Wilson K, Homan K, Emelianov S. Biomedical photoacoustics beyond thermal expansion using triggered nanodroplet vaporization for contrast-enhanced imaging. Nat Commun. 2012; 3: 618.

26. Lee N, Yoo D, Ling D, et al. Iron Oxide Based Nanoparticles for Multimodal Imaging and Magnetoresponsive Therapy. Chem Rev. 2015; 115: 10637-89.

27. Stocker A, Hilbers ML, Gauthier C, et al. HER2/CEP17 Ratios and Clinical Outcome in HER2-Positive Early Breast Cancer Undergoing Trastuzumab-Containing Therapy. PLoS One. 2016; 11: e0159176.

28. Kaneda MM, Caruthers S, Lanza GM, et al. Perfluorocarbon nanoemulsions for quantitative molecular imaging and targeted therapeutics. Ann Biomed Eng. 2009; 37: 1922-33.

29. Woodrow KA, Cu Y, Booth CJ, et al. Intravaginal gene silencing using biodegradable polymer nanoparticles densely loaded with small-interfering RNA. Nat Mater. 2009; 8: 526-33.

30. Wang H, Agarwal P, Zhao S, et al. Hyaluronic acid-decorated dual responsive nanoparticles of Pluronic F127, PLGA, and chitosan for targeted co-delivery of doxorubicin and irinotecan to eliminate cancer stem-like cells. Biomaterials. 2015; 72: 74-89.

31. Zhao Y, Song W, Wang D, et al. Phase-Shifted PFH@PLGA/Fe3O4Nanocapsules for MRI/US Imaging and Photothermal Therapy with near-Infrared Irradiation. ACS Appl Mater Interfaces. 2015; 7: 14231-42.

32. Lin LS, Cong ZX, Cao JB, et al. Multifunctional Fe3O4@Polydopamine Core Shell Nanocomposites for Intracellular mRNA Detection and Imaging-Guided Photothermal Therapy. ACS Nano. 2014; 8: 3876–83.

33. Lin J, Wang M, Hu H, et al. Multimodal-Imaging-Guided Cancer Phototherapy by Versatile Biomimetic Theranostics with UV and gamma-Irradiation Protection. Adv Mater. 2016; 28: 3273-9.

34. Lee N, Cho HR, Oh MH, et al. Multifunctional Fe3O4/TaO(x) core/shell nanoparticles for simultaneous magnetic resonance imaging and X-ray computed tomography. J Am Chem Soc. 2012; 134: 10309-12.

35. Muthana M, Kennerley AJ, Hughes R, et al. Directing cell therapy to anatomic target sites in vivo with magnetic resonance targeting. Nat Commun. 2015; 6: 8009.

36. You Y, Wang Z, Ran H, et al. Nanoparticle-enhanced synergistic HIFU ablation and transarterial chemoembolization for efficient cancer therapy. Nanoscale. 2016; 8: 4324-39.

37. Guo M, Huang J, Deng Y, et al. pH-Responsive Cyanine-Grafted Graphene Oxide for Fluorescence Resonance Energy Transfer-Enhanced Photothermal Therapy. Adv Funct Mater. 2015; 25: 59-67.

38. Song X, Feng L, Liang C, et al. Ultrasound Triggered Tumor Oxygenation with Oxygen-Shuttle Nanoperfluorocarbon to Overcome Hypoxia-Associated Resistance in Cancer Therapies. Nano Lett. 2016; 16: 6145-53.

39. Roper DK, Ahn W, Hoepfner M. Microscale Heat Transfer Transduced by Surface Plasmon Resonant Gold Nanoparticles. J Phys Chem C Nanomater Interfaces. 2007; 111: 3636-41.

40. Hessel CM, Pattani VP, Rasch M, et al. Copper selenide nanocrystals for photothermal therapy. Nano Lett. 2011; 11: 2560-6.

41. Tao W, Ji X, Xu X, et al. Antimonene Quantum Dots: Synthesis and Application as Near-Infrared Photothermal Agents for Effective Cancer Therapy. Angew Chem Int Ed Engl. 2017; 56: 11896-900.

42. Zhu L, Wang D, Wei X, et al. Multifunctional pH-sensitive superparamagnetic iron-oxide nanocomposites for targeted drug delivery and MR imaging. J Control Release. 2013; 169: 228-38.

43. Lion M, Harle A, Salleron J, et al. Trastuzumab as a preoperative monotherapy does not inhibit HER2 downstream signaling in HER2-positive breast cancer. Oncol Lett. 2016; 12: 2028-32.

44. Singh N, Jenkins GJ, Asadi R, et al. Potential toxicity of superparamagnetic iron oxide nanoparticles (SPION). Nano Rev. 2010; 1.

45. Stylianopoulos T, Jain RK. Design considerations for nanotherapeutics in oncology. Nanomedicine. 2015; 11: 1893-907.

46. Levy M, Luciani N, Alloyeau D, et al. Long term in vivo biotransformation of iron oxide nanoparticles. Biomaterials. 2011; 32: 3988-99.

47. Corot C, Robert P, Idee JM, et al. Recent advances in iron oxide nanocrystal technology for medical imaging. Adv Drug Deliv Rev. 2006; 58: 1471-504.

48. Guo W, Guo C, Zheng N, et al. Csx WO3 Nanorods Coated with Polyelectrolyte Multilayers as a Multifunctional Nanomaterial for Bimodal Imaging-Guided Photothermal/Photodynamic Cancer Treatment. Adv Mater. 2017; 29.

49. Shibu ES, Hamada M, Murase N, et al. Nanomaterials formulations for photothermal and photodynamic therapy of cancer. J Photochem Photobiol C. 2013; 15: 53-72.

50. Kim BY, Rutka JT, Chan WC. Nanomedicine. N Engl J Med. 2010; 363: 2434–43.

51. Shi J, Kantoff PW, Wooster R, et al. Cancer nanomedicine: progress, challenges and opportunities. Nat Rev Cancer. 2017; 17: 20-37.

52. Tong R, Langer R. Nanomedicines Targeting the Tumor Microenvironment. Cancer J. 2015; 21: 314–21.

53. Jaque D, Martínez Maestro L, del Rosal B, et al. Nanoparticles for photothermal therapies. Nanoscale. 2014; 6: 9494-530.

54. Perrault SD, Walkey C, Jennings T, et al. Mediating Tumor Targeting Efficiency of Nanoparticles Through Design. Nano Lett. 2009; 9: 1909–15

55. Allen TM, Hansen C, Martin F, et al. Liposomes containing synthetic lipid derivatives of poly (ethylene glycol) show prolonged circulation half-lives in vivo. Biochim Biophys Acta. 1991; 1066: 29-36.

56. Papahadjopoulos D , Allen TM, Gabizon A, et al. Sterically stabilized liposomes—improvements in pharmacokinetics and antitumor therapeutic efficacy. Proc Natl Acad Sci U S A. 1991; 88: 11460-4.

57. Prabhakar U, Maeda H, Jain RK, et al. Challenges and key considerations of the enhanced permeability and retention effect for nanomedicine drug delivery in oncology. Cancer Res. 2013; 73: 2412-7.

58. Stefan W, Anthony JT, Qin D, et al. Analysis of nanoparticle delivery to tumours. Nat Rev Mater. 2016; 1: 16014.

59. Jain RK, Stylianopoulos T. Delivering nanomedicine to solid tumors. Nat Rev Clin Oncol. 2010; 7: 653-64.

60. Sugahara KN, Teesalu T, Karmali PP, et al. Tissue-penetrating delivery of compounds and nanoparticles into tumors. Cancer Cell. 2009; 16: 510-20.

61. Huang SK, Martin FJ, Jay G, et al. Extravasation and transcytosis of liposomes in Kaposi's sarcoma–like dermal lesions of transgenic mice bearing the HIV tat gene. Am J Pathol. 1993; 143: 10-4.

62. Pirollo KF, Chang EH. Does a targeting ligand influence nanoparticle tumor localization or uptake? Trends Biotechnol. 2008; 26: 552-8.

63. Arnal B, Perez C, Wei CW, et al. Sono-photoacoustic imaging of gold nanoemulsions: Part I. Exposure thresholds. Photoacoustics. 2015; 3: 3-10.

64. Arnal B, Wei CW, Perez C, et al. Sono-photoacoustic imaging of gold nanoemulsions: Part II. Real time imaging. Photoacoustics. 2015; 3: 11-9.

65. Dove JD, Mountford PA, Murray TW, et al. Engineering optically triggered droplets for photoacoustic imaging and therapy. Biomed Opt Express. 2014; 5: 4417-27.

66. Ullrich E, Bonmort M, Mignot G, et al. Tumor stress, cell death and the ensuing immune response. Cell Death Differ. 2008; 15: 21-8.